BIOPHYSICS AND BASIC BIOMEDICAL RESEARCH – Full Papers

Magnetic Resonance in Medicine 76:259–269 (2016)

Exploring Multifractal-Based Features for Mild Alzheimer's Disease Classification

Huangjing Ni,[1,2] Luping Zhou,[2] Xinbao Ning,[1] and Lei Wang,[2]*
for the Alzheimer's Disease Neuroimaging Initiative (ADNI)

Purpose: Multifractal applications to resting state functional MRI (rs-fMRI) time series for diagnosing Alzheimer's disease (AD) are still limited. We aim to address two issues: (I) if and what multifractal features are sufficiently discriminative to detect AD from the healthy; (II) if AD classification could be further improved by combining multifractal features with traditional features in this field.

Methods: Rs-fMRI data of 25 AD patients and 38 normal controls were analyzed. A set of multifractal features were systematically investigated. Traditional features in monofractal, linear, and network-based categories were also extracted for comparison and combination. Both support vector machines and multiple kernel learning (MKL) were used to perform classification with individual and combined features.

Results: We identified a multifractal feature, Δf, which has the strongest discriminative power among all the features in our study. Moreover, we found that the classification accuracy could be significantly improved from 69% (by Δf only) to up to 76%, when nonsparse MKL is used to combine Δf with the monofractal feature, Hurst. Finally, we showed that incorporating other multifractal features, $\alpha(0)$, $\Delta\alpha$ and P_c, could also improve traditional-feature-based AD classification.

Conclusion: Our work demonstrated the potential usefulness of multifractal analysis for AD research, especially when combining with the traditional rs-fMRI features. It contributes to distinguishing AD from NC subjects. **Magn Reson Med 76:259–269, 2016. © 2015 Wiley Periodicals, Inc.**

Key words: multifractal; Alzheimer's disease; classification; multiple kernel learning

INTRODUCTION

Alzheimer's disease (AD) is a progressive neurodegenerative disorder, resulting in a gradual, irreversible loss of memory and cognitive function and affecting millions of people around the world (1). Early and accurate diagnosis of AD is not only challenging but also crucial from the perspective of future treatments. Noninvasive neuroimaging techniques such as functional MRI (fMRI) are commonly used to diagnose and monitor the progression of the disease and the effect of the treatment. Moreover, resting state fMRI (rs-fMRI) can reflect spontaneous neuronal activities (2) and the endogenous neurophysiological process of human brain (3). Because neither stimulation nor response is required, the images can be easily collected for subjects, especially patients. Hence, rs-fMRI has received increasing interest in AD related studies recently (4–6). Prevailing investigations on studying AD with rs-fMRI data are mainly focused on linear correlation analysis, such as regional homogeneity (ReHo) (6), amplitude of low frequency fluctuations (ALFF) (7), and fractional ALFF (fALFF) (8), as well as functional connectivity analysis (9). Through univariate statistical tests, significant group differences can be identified from spatially normalized brain images. These analyses assume that rs-fMRI time series were temporally stationary, while recent studies have demonstrated that rs-fMRI time series show complex and locally variable autocorrelation structures (10). Moreover, the disease-induced alterations, particularly at the early stage of AD, may be subtle and thus difficult to be captured by the traditional linear approaches. Hence, nonlinear methods should be considered in this case. Since Zarahn et al (11) and Shimizu et al (12) demonstrated that the power spectrum of rs-fMRI can be well characterized by the $1/f$ function, a consensus has been reached that rs-fMRI time series with long-term autocorrelation and self-similarity can be described by fractal measures in both spatial and temporal domains (10,13–16).

Fractals can be classified as monofractal and multifractals depending on the number of indexes needed to characterize their scaling properties. Only a single scaling exponent is used in monofractal analysis to describe the behavior in the whole time series. However, the behaviors of the brain system are too complex to be adequately modeled by one exponent. Comparatively, multifractals, which can be deemed as a superposition of homogeneous monofractal structures (17), are more appropriate for analyzing such a process. The multifractal formalism was primarily established to account for the statistical scaling properties of singular measures arising in physics and medicine (18). A measure is called singular if it cannot be expressed by either a density function or a sum of Dirac distributions (12). The essence of multifractal analysis is to model the singularities of a fractal signal by their degree of effect on the global structure (12) and to produce the distribution of indices of regularity, which

[1]School of Electronic Science and Engineering, Nanjing University, Nanjing, China.

[2]School of Computer Science and Software Engineering, University of Wollongong, Wollongong, NSW, Australia.

*Correspondence to: Dr. Wang, School of Computer Science and Software Engineering, University of Wollongong, Wollongong NSW 2522, Australia. E-mail: leiw@uow.edu.au

Received 25 November 2014; revised 28 June 2015; accepted 29 June 2015

DOI 10.1002/mrm.25853
Published online 20 July 2015 in Wiley Online Library (wileyonlinelibrary.com).

© 2015 Wiley Periodicals, Inc.

constitutes the multifractal spectrum (MFS). Evidence for the presence of multifractality in both resting state and task related fMRI signals has been demonstrated in almost the whole brain. For example, Shimizu et al (12) found multifractal structures in white and gray matter, and the significant differences in the singularity spectra between the activated and the nonactivated brain regions. Wink et al (15) conducted multifractal analysis on rs-fMRI time series in the right inferior frontal cortex and revealed that the faster responding participants had wider MFS. Ciuciu et al (16) applied multifractal analysis to both resting state network (RSN) and non-RSN structures, and found that rs-fMRI signals appear multifractal in almost all brain regions except the noncortical ones.

Although some progresses of multifractal analysis in rs-fMRI time series have been made, multifractal applications to rs-fMRI time series for AD research have not been well studied. Meanwhile, the dominant mass univariate methods are of limited utility at a group level (19). Machine learning methods have been applied to this field to facilitate multivariate analysis for individuals and achieved many successful results. Therefore, it is sensible and of great significance to integrate multifractal analysis and machine learning methods for AD research. Furthermore, in addition to single classifiers, such as support vector machines (SVM) (20), pseudo-fisher linear discriminative analysis (21), and random forests (22), multiple kernel learning (MKL), which is a popular feature fusion and/or modality fusion tool, has recently been used to integrate the complementary information for effective AD detection (23,24). We hereby use MKL algorithms to fuse various feature categories to improve the performance of AD diagnosis.

Extracting representative and discriminative features can significantly improve the performance in AD classification. Meanwhile, the classification performances for the patients or clinicians can be improved by removing the redundant and irrelevant features during the feature selection process. As we will show, many multifractal features can be extracted from MFS. Do they have sufficient discriminative power for AD diagnosis? Can their discriminative power be further improved when they are combined with other more traditional features, i.e., monofractal, linear, and/or network-based ones? To the best of our knowledge, there is no sufficient research on this topic yet. We hereby conducted a systematic study on multifractal features for AD classification and devoted to addressing two issues: (Issue-I) if and what multifractal features are sufficiently discriminative in detecting AD from the healthy on rs-fMRI data; (Issue-II) if the discriminative performance could be further enhanced by combining multifractal features with traditional features used in this field.

The rest of the article is organized as follows: the Methods section provides the information on participants and data preprocessing. It is followed by an introduction to multifractal feature extraction. Afterward, how discriminative features are selected and fused by means of the MKL technique is described. The aforementioned Issue-I and Issue-II are investigated in the Results section. Interesting findings are then presented and discussed extensively in the Discussion section. The Conclusions section concludes this article.

METHODS

An overview of our study is shown in Figure 1 and described as follows.

I. For each subject, the rs-fMRI time series from each of the regions of interest (ROI) were preprocessed (see the Data Preprocessing section) to extract various feature categories.
II. Based on the preprocessed rs-fMRI images, a set of features was extracted from four feature categories, namely the multifractal, the monofractal, the linear, and the network-based categories. Each category was further comprised of multiple features. In particular, four multifractal features were proposed in the Feature Extraction from MFS section, to characterize MFS for AD detection.
III. Discriminative ROIs were identified by a feature selection process applied to individual feature types (the Discriminative Feature Selection section).
IV. After feature selection, two kinds of classifiers were used for AD classification: SVM on each individual feature type, and MKL on the combined feature types.

Participants

Rs-fMRI data used in this study were downloaded from the Alzheimer's Disease Neuroimaging Initiative (ADNI) database. The introductions of ADNI can be found in part A of the Supporting Information, which is available online.

Fifty-nine subjects including 25 patients with AD and 38 normal controls (NC) were analyzed in this study. Although not all the subjects were recorded with Mini-Mental State Examination scores, all of them had a diagnosed label. The data were acquired on a 3.0 Tesla (T) MRI scanner (Philips) with repetition time/echo time (TR/TE) as 3000/30 ms and flip angle (FA) of 80°. Each series had 140 volumes, and each volume consisted of 48 image slices with dimensions 64×64 and voxel size $3.31 \times 3.31 \times 3.31$ mm^3. Sagittal structural images with a resolution of $1 \times 1 \times 1.2$ mm^3 were acquired using a magnetization prepared rapid gradient echo (MPRAGE) three-dimensional T1-weighted sequence (repetition time [TR] = 6.8 ms; echo time [TE] = 3.16 ms; FA = 9°). The demographic information about the participants was summarized in Table 1.

Data Preprocessing

All functional imaging data preprocessing was performed using Data Processing Assistant for Resting-State fMRI Advanced Edition (25), which is based on Statistical Parametric Mapping (SPM8) (26). The first 10 volumes were discarded to remove possible T1 stabilization effects. After slice timing, images were realigned for head motion and distortion corrections. The functional brain images were then normalized to the Montreal Neurological Institute space using unified segmentation on their respective anatomical data and spatially smoothed with a 4 mm full-width at half-maximum isotropic

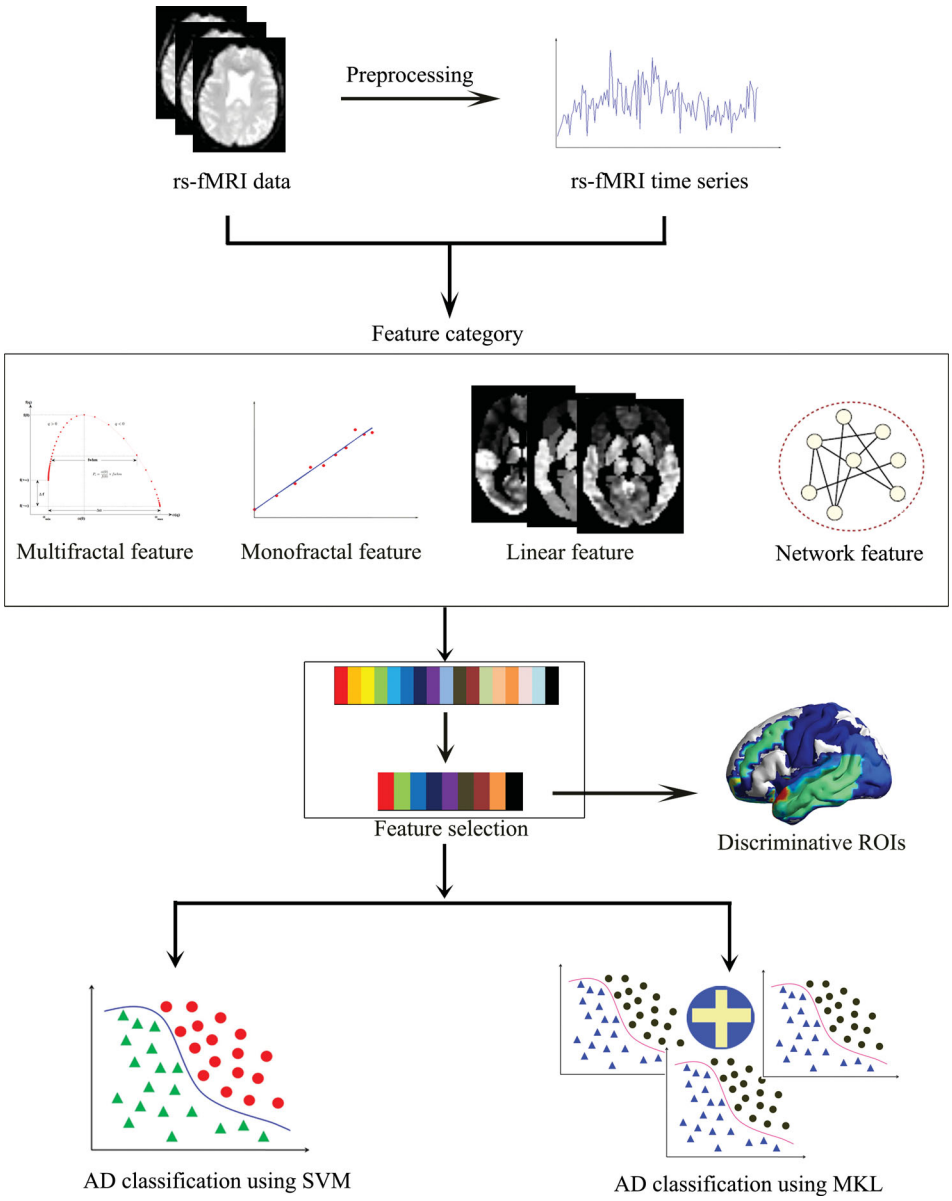

FIG. 1. Overview of the proposed approach.

Gaussian kernel. Afterward, regressions of nuisance signals including white matter, cerebrospinal fluid signals and six head-motions were performed on functional images. Because de-trending and filtering are often dismissed in multifractal fMRI analysis (12,15,16) but used for linear and network features (6,7,9), to better align with these literatures, de-trending linear drift and temporal filter (0.01–0.08 Hz) were then only performed for ReHo, ALFF, and ROI-wise functional connectivity calculation. Finally, the preprocessed images were parcellated into 90 cerebral ROIs in the Automated Anatomical Labeling (AAL) atlas (27) and the regional mean time series of each ROI was extracted for fractal analysis. To be noted, ReHo values were calculated without spatial smoothing.

Table 1
Demographic Information of the Subjects Involved in This Study

	NC	AD
No. subjects (n)	34	25
Age (years)	76.5 ± 6.4	73.7 ± 7.6
Gender(male/female)	11/23	11/14
No. of subjects with MMSE	24	11
Baseline MMSE	29.3 ± 0.9	21.3 ± 3.8

NC = normal controls; AD = Alzheimer's disease; MMSE = Mini-Mental State Examination; plus-minus values are mean ± SD.

Multifractal Analysis and Feature Extraction

The simplest type of multifractal analysis is to use the classical box counting based multifractal analysis (BCMA) to estimate MFS through the concept of singularity. Despite its conceptual simplicity and popularity, BCMA may find multifractality even on a monofractal process, while this could be better handled by wavelet transform based approaches (28–30). These approaches

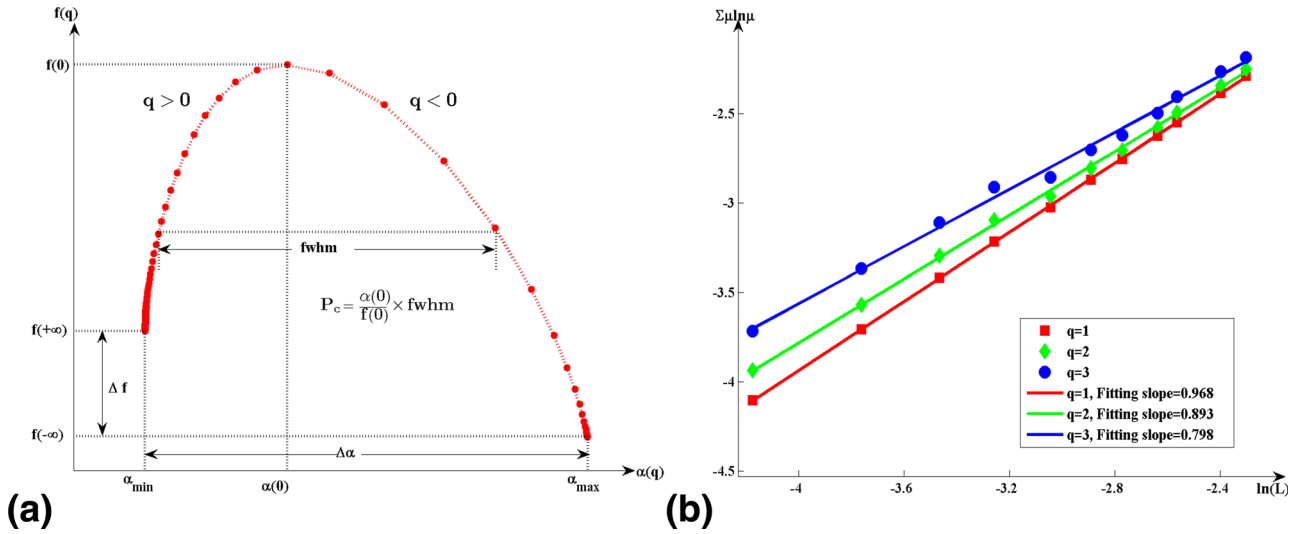

FIG. 2. **a**: Illustration of the features extracted from a multifractal spectrum using BCMA. **b**: Illustration of verifying multifractal characteristics in BCMA. The square, diamond, and dot symbols correspond to the cases of q = 1, q = 2, and q = 3, respectively. In each case, linear fitting is performed and shown with the solid line, and its slope value is given in the legends. No ambiguity in the determination of the three different slopes suggests the multifractal characteristics in the rs-fMRI series.

mainly focus on the wavelet transform modulus maxima method and the wavelet leaders based multifractal analysis (WLMA). Previous studies have demonstrated that the wavelet leader can better capture the multifractal behaviors in multi-resolution quantity than the wavelet coefficient in wavelet domain, and hence WLMA is recommended (28,31). However, it is observed in our study that WLMA does not work well on short time series (see the supporting information part H). Reasonable MFS cannot be obtained with WLMA in certain ROIs for some subjects by using short time series. Comparatively, BCMA seems to be more robust in such a situation. In light of this, we use both WLMA and BCMA to verify the multifractality in rs-fMRI to avoid potential misjudgements, but use BCMA to extract MFS-based features for our analysis. The fundamentals of BCMA and WLMA are introduced in supporting information part B and part C.

Feature Extraction from MFS

Although various features can be extracted from MFS by using BCMA, we mainly focus on four canonical features, namely, $\alpha(0)$, $\Delta\alpha$, Δf and P_c. These features are illustrated in Figure 2a.

The feature $\alpha(0)$ represents the most common singularity index found within a time series, which can describe the MFS mode. It is a measure of the overall relative persistence of the time series. When the moment variate $q = 0$, the corresponding singularity value $\alpha(0)$ can be determined through the apex of the spectrum $f(0)$. The higher the $\alpha(0)$ value is, the relatively more persistent the time series becomes, and vice-versa.

The feature $\Delta\alpha = \alpha_{max} - \alpha_{min}$ represents the width of the MFS, which can detect the degree of multifractality of the time series. In BCMA (32,33), the probability in the i-th box can be measured by $P_i \propto L^{\alpha_i}$, where L (usually $0 < L \leq 1$) is the box size and α_i is the singularity strength of the probability subset. Also, α_{max} is related to the minimum probability measure by means of $P_{min} \propto L^{\alpha_{max}}$, whereas α_{min} is related to the maximum probability measure by means of $P_{max} \propto L^{\alpha_{min}}$. The $\Delta\alpha$ can thus be used to describe the range of the probability measures through $P_{max}/P_{min} \propto (1/L)^{\Delta\alpha}$. The greater the $\Delta\alpha$ value is, the broader the probability distribution, the richer the structure and the stronger the degree of multifractality in the time series.

The feature $\Delta f = f(+\infty) - f(-\infty)$ represents the difference of fractal dimension. In BCMA (32,33), $f(+\infty)$ reflects the fractal dimension of the subset of the maximum probability with $N_{P_{max}} = N_{\alpha_{min}} \propto L^{-f(+\infty)}$, where $N_{P_{max}}$ and $N_{\alpha_{min}}$ are the number of boxes of the size L $(0 < L \leq 1)$ with the same maximum probability. $f(-\infty)$ reflects the fractal dimension of the minimum probability such that $N_{P_{min}} = N_{\alpha_{max}} \propto L^{-f(-\infty)}$, where $N_{P_{min}}$ and $N_{\alpha_{max}}$ are the number of boxes of the size L $(0 < L \leq 1)$ with the same minimum probability. Hence, the Δf value can describe the ratio between the most concentrated and the most rarified regions of the probability measure: $N_{P_{max}}/N_{P_{min}} \propto (1/L)^{\Delta f}$. Thus, $\Delta f > 0$ signifies that there are more concentrated regions than rarified sites, whereas $\Delta f < 0$ signifies the contrary and $\Delta f = 0$ indicates the equiprobability for both concentrated and rarified regions. In addition, Δf can also be used to measure the shape of the MFS to a great extent. Specifically, $\Delta f > 0$ corresponds to the MFS with left skewness (as shown in Figure 2a), whereas $\Delta f < 0$ corresponds to the right skewed MFS shape, and $\Delta f = 0$ corresponds to a symmetrical bell-jar shape.

The feature P_c, as a compound measure, is introduced to allow a better separation of different time series characteristics. It can be calculated by $\alpha(0)$, $f(0)$ and the full-width-at-half-maximum (fwhm) value from MFS as $P_c = \frac{\alpha(0)}{f(0)} \times fwhm$. It will give low values for simple

white Gaussian noise time series, and high value for the time series containing more complex properties (12).

MKL for Feature Fusion

MKL approach is used to combine the multifractal characteristics and other classical features with appropriate weighting. MKL defines a set of base kernels and learns the optimal combination weights for these base kernels. MKL allows to use different types of kernels or features concurrently in a single classifier. It has recently been applied to AD study and achieved successful results (24,34,35). Specifically, in our case, the commonly used kernels with different parameters are used as the base kernels. Let $X_i = \{\mathbf{x}_{if} | f = 1, \cdots, F\}$ be the feature set of the i-th subject, where $\mathbf{x}_{if}$ represents the f-th feature vector extracted from the 90 ROIs, and F the total number of the types of features. Assigning each feature type with M base kernels, we can represent MKL as:

$$K(X_i, X_j) = \sum_{f=1}^{F} \sum_{m=1}^{M} d_{fm} K_{fm}(\mathbf{x}_{if}, \mathbf{x}_{jf}),$$

where d_{fm} is a weight coefficient of the m-th base kernel for the f-th feature, and $K_{fm}(\mathbf{x}_{if}, \mathbf{x}_{jf})$ is a base kernel function. The weight coefficient can naturally reflect the importance of each base kernel when they are appropriately normalized to become comparable to each other. In existing neuroimaging applications, ℓ_1-MKL is usually used, which can be efficiently solved by simpleMKL (36). It imposes the constraint $\{\sum_{f=1}^{F} \sum_{m=1}^{M} d_{fm} = 1, d_{fm} \geq 0, \forall f, m\}$ to make the optimal solution d_{fm} sparse. Several kernel combination weights in the optimal solution will be zeros, indicating that the corresponding base kernels are essentially not used, and ℓ_1-MKL can thus be used to select the important kernels for a given task. However, ℓ_1-MKL is not always beneficial in practice and sometimes may become even less effective when the base kernels carry complementary information (37). In such a situation, nonsparse MKL, called ℓ_p-MKL, is usually a better option (38). Compared with ℓ_1-MKL, ℓ_p-MKL ($p \geq 2$) imposes a constraint $\{||d||_p \leq 1, d_{f,m} \geq 0\}$. It has been demonstrated in Kloft et al (39) that ℓ_1-MKL is better when the base kernels contain a large amount of redundant information, and ℓ_p-MKL is preferred otherwise.

Discriminative Feature Selection

For a certain feature type (e.g., $\Delta\alpha$), we can calculate its value on each of the 90 cerebral ROIs in AAL atlas and thus a 90-dimensional feature vector can be obtained for each subject to perform classification. However, the 90 ROI features are not equally discriminative for AD classification. Including less discriminative ROIs may not only waste computation resources, but also deteriorate the classification accuracy due to the presence of redundant and irrelevant features. Therefore, feature selection techniques have been widely used to select discriminative ones from a pool of features to improve the classification performance for a given task.

Considering the interactions between the ROIs, the commonly used sequential backward selection (SBS) algorithm is adopted in this study. It aims to select an optimal subset of features that can optimize the performance of SVM classifier. The working of SBS is introduced in part E of the supporting information. In our work, SBS feature selection is embedded into the commonly used leave-one-out (LOO) classification scheme to make a full use of the limited number of subjects in our dataset. The LOO scheme works as follows. Each of the N subjects in our study will be reserved as the (only) test sample in turn, while the remaining N-1 subjects are used as the training samples correspondingly. In this way, this scheme leads to N classification tasks in total. In each of these tasks, ROIs are selected by carrying out the SBS feature selection. The feature values extracted from the selected ROIs are then concatenated to form feature vectors for classification.

Because different training data are used in each task in LOO, SBS may select different ROIs each time. The more frequently an ROI is selected over the N classification tasks, the more important it is regarded for classification. The selection frequency is measured by W-score, calculated as $W(i) = \sum_{n=1}^{N} \sum_{f=1}^{F} B_{nf}(i)/(N * F)$, where i is the index of ROI, and N F have been previously defined. The binary indicator $B_{nf}(i)$ indicates the selection status (1 for "selected" and 0 for "not selected") of the i-th ROI in the n-th task with the f-th feature type. Ranking the discriminative power of ROIs with W-score identifies disease-related brain regions with respect to the used feature types. Also, it could provide the comparison with the documented reports for sanity check or new discovery.

Test on Individual and Combined Features

Based on the four canonical multifractal features extracted from MFS by BCMA, i.e., $\alpha(0)$, $\Delta\alpha$, Δf and P_c, the SVM classifier with a Gaussian radial basis function (GRBF) kernel was applied to investigate if and what multifractal features are sufficiently discriminative in detecting AD from the healthy on rs-fMRI time series. Classification accuracy, sensitivity, and specificity were adopted to evaluate the diagnostic power for individual feature types.

To test (i) whether complementary information exists between multifractal features and the traditional ones, and (ii) whether the classification accuracy could be further improved, MKL technique was used to combine the features together. All the four multifractal features, $\alpha(0)$, $\Delta\alpha$, Δf and P_c, were combined with the traditional features, Hurst, ReHo, ALFF, fALFF, and wLCC. Classification accuracy, sensitivity, and specificity are also used to evaluate the combined features.

RESULTS

To address the Issue I and Issue II in the Introduction section, we conducted the following experiments: (i) For comparison and combination, we calculated the monofractal feature, Hurst exponent (40); three representative linear indices, ReHo (6), ALFF (7), and fALFF (8); and functional connectivity (9) based feature wLCC (41). The

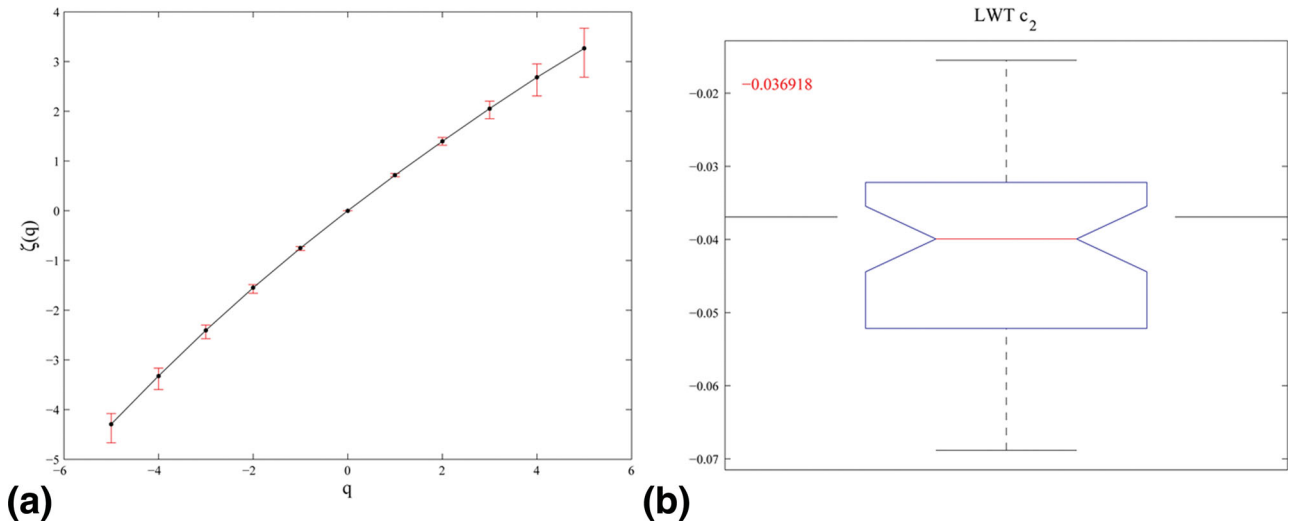

FIG. 3. **a**: Illustration of the scaling function obtained by WLMA. **b**: Illustration of the estimation of c_2 by WLMA for an rs-fMRI time series. Both subfigures are based on the bootstrap technology with the resample number being 49. The departure of $\zeta(q)$ from a linear behavior in q and also the coefficient $c_2 \neq 0$ suggest the multifractal characteristics in the rs-fMRI series.

extraction of these features can be found in part D in the supporting information. (ii) We verified the multifractality in rs-fMRI time series using both BCMA and WLMA. (iii) We applied the SVM classifier to individual feature classification. (iv) We used both ℓ_1-MKL and ℓ_p-MKL ($p = 2,3$) to test the discriminative performance on combined features.

More details of the experimental settings can be found in part G of the supporting information.

Multifractal Characteristics Verification

Based on the processed rs-fMRI time series, we verified their multifractal characteristics by BCMA first. We plotted three fitted lines of $\sum \mu_i \ln \mu_i$ versus $\ln L$ with $q = 1, 2, 3$, as illustrated in Figure 2b, where the symbols μ_i is the normalized q-th moment of the probability and L is the segmented box size. The significant differences among the three fitting slopes suggest the presence of multifractal characteristics in rs-fMRI time series. In addition, to avoid the potential mis-judgements of BCMA, the multifractality is further verified by using WLMA. An illustration is shown in Figure 3 and the symbols are defined in the supporting information Part C. Using bootstrap technique with the number of resample being 49, the scaling function $\zeta(q)$ of the statistical order q and the log-cumulant coefficient c_2^L can be estimated by WLMA. It is obvious that $\zeta(q)$ is not a linear function of q and the confidence interval for c_2^L excludes the zero value, which is in line with the multifractal characteristic. Therefore, the multifractality in the rs-fMRI time series is verified by using both BCMA and WLMA. Also, as a side note, WLMA may not work well on short time series (see part H of the supporting information) and reasonable MFS could not always be obtained in our experiment, which is not this case for

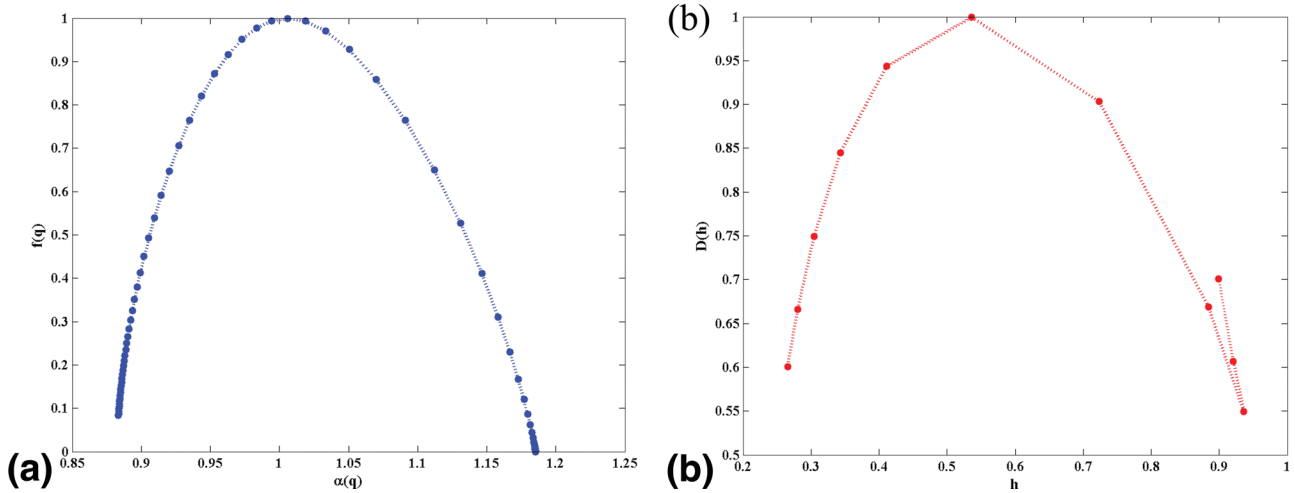

FIG. 4. **a**: Illustration of MFS obtained by BCMA. **b**: Illustration of MFS obtained by WLMA on the same ROI for the same subject. This figure is shown to illustrate that a reasonable MFS could not always be obtained with WLMA in certain ROIs for some subjects in our experiment.

Table 2
SVM with a GRBF Kernel Classification Performance (in Percentage) on Each Individual Feature

Feature categories	Features	Accuracy	Sensitivity	Specificity
Multifractal	$\alpha(0)$	52.54	42.11	57.50
	$\Delta\alpha$	52.54	42.11	57.50
	Δf	**69.49**	**64.00**	**73.53**
	P_c	59.32	51.85	65.63
Monofractal	Hurst	64.41	58.33	68.57
Linear	ReHo	57.63	50.00	61.54
	ALFF	49.15	27.27	54.17
	fALFF	61.02	54.55	64.86
Network-based	wLCC	61.02	57.14	62.22

BCMA. An illustration of MFS obtained by BCMA and WLMA on the same ROI for the same subject is shown in Figure 4. Because BCMA was found empirically more robust than WLMA on the short rs-fMRI time series, we, therefore, extracted features on the MFS produced by BCMA for the subsequent analysis.

Test on Individual Features (Issue-I)

As can be observed in Table 2, Δf appears to be the most discriminative individual feature and significantly outperforms the others with an accuracy of 69.49%, a sensitivity of 64.00% and a specificity of 73.53%. In addition, the monofractal, linear, and network-based features were also used for classification. From Table 2, Hurst exponent presents as the second best feature, while fALFF and wLCC also show relatively good accuracy higher than 60.00%. Generally, Δf, as the representative of multifractal feature category, outperforms those from the other three feature categories.

Test on Combined Features (Issue-II)

As shown in Table 3, applying MKL to feature fusion can enhance the classification performance in general and we have the following observations. (i) All multifractal features can help improve the performances of the other five traditional features, except that $\alpha(0)$+fALFF, $\Delta\alpha$+fALFF, and $\Delta\alpha$+wLCC show degraded performance and that $\Delta\alpha$+Hurst maintains the previous performance. When choosing the best combination based on classification accuracy, we end up with the fusion between Δf and Hurst. It reaches the highest accuracy of 76.27% with the sensitivity of 72.00% and the specificity of 79.41%. At the same time, it is worth noting that the following four fusion settings, P_c+wLCC, $\alpha(0)$+ReHo, P_c+Hurst, and $\alpha(0)$+Hurst, are equally good as Δf+Hurst in the statistical sense. (ii) Compared with the other three multifractal features, P_c can significantly enhance the performance of the traditional features, as observed in P_c+Hurst, P_c+ReHo, P_c+ALFF, P_c+fALFF, and P_c+wLCC. These combined features boost the accuracies by 6.78%, 11.86%, 15.26%, 1.69%, and 8.47%, respectively, better than any individual conventional features. (iii) Most of the best classification results are obtained by using GRBF+Poly kernel. (iv) Better performance is usually achieved by ℓ_p-MKL rather than ℓ_1-MKL.

Discriminative ROIs

Using the feature selection method, we identified the most discriminative ROIs for both individual and combined features. For illustration, we presented results for the best individual feature type Δf (Table 4) and the best feature combination Δf+Hurst (Table 5).

The top 15 ROIs are listed in descending order of their W-score values. For both Δf and Δf+Hurst, the shared top discriminative ROIs include the left amygdala

Table 3
Best Classification Performance (in Percentage) on Combined Features Using MKL with Different Combination Types of Base Kernels

Feature combination	ACC	SEN	SPE	CombType	Norm
Δf+Hurst	**76.27**	**72.00**	**79.41**	**C2**	**L2, L3**
Δf+ReHo	62.71	56.52	66.67	C1, C2, C3, C4	L2, L3
Δf+ALFF	61.02	55.00	64.10	C2	L2
Δf+fALFF	66.10	61.90	68.42	C1	L3
Δf+wLCC	67.80	65.00	69.23	C2	L2
P_c+Hurst	**71.19**	**65.38**	**75.76**	**C3, C4**	**L2, L3**
P_c+ReHo	**69.49**	**68.42**	**70.00**	**C2**	**L2**
P_c+ALFF	**64.41**	**64.29**	**64.44**	**C3**	**L1, L2, L3**
P_c+fALFF	**62.71**	**57.89**	**65.00**	**C2**	**L3**
P_c+wLCC	**69.49**	**66.67**	**71.05**	**C1**	**L1**
$\alpha(0)$+Hurst	**71.19**	**66.67**	**74.29**	**C2**	**L3**
$\alpha(0)$+ReHo	**72.88**	**90.91**	**68.75**	**C1**	**L3**
$\alpha(0)$+ALFF	50.85	0	54.55	C2, C3, C4	L2, L3
$\alpha(0)$+fALFF	57.63	50.00	58.49	C2	L3
$\alpha(0)$+wLCC	**62.71**	**71.43**	**61.54**	**C2**	**L3**
$\Delta\alpha$+Hurst	64.41	59.09	67.57	C1, C2, C3, C4	L1
$\Delta\alpha$+ReHo	**61.02**	**62.50**	**60.78**	**C4**	**L2, L3**
$\Delta\alpha$+ALFF	**54.24**	**37.50**	**56.86**	**C2**	**L2**
$\Delta\alpha$+fALFF	57.63	50.00	58.82	C4	L2, L3
$\Delta\alpha$+wLCC	57.63	50.00	58.18	C1, C2	L1

ACC = accuracy; SEN = sensitivity; SPE = specificity; CombTypes = combination types; C1 = GRBF kernel; C2 = GRBF+Poly kernel; C3 = GRBF+Lap+Invs+Invd kernel; C4 = GRBF+Poly+Lap+Invs+Invd kernel; L1 = Sparse ℓ_1-MKL; L2, L3 = Non-sparse ℓ_p-MKL ($p = 2, 3$). It is highlighted in bold for the better performances of combined features than those of individual ones in Table 3.

Table 4
Top 15 ROIs Showing the Most Discriminative Power for Classification by Δf Feature[a]

No.	Regions	*W*-score
1	Left amygdala	0.8983
2	Right middle temporal gyrus	0.8644
3	Right inferior occipital gyrus	0.7966
4	Left temporal pole: superior temporal gyrus	0.7797
5	Right temporal pole: middle temporal gyrus	0.7288
6	Left superior frontal gyrus, orbital part	0.5593
7	Right inferior temporal gyrus	0.5424
8	Right superior frontal gyrus, orbital part	0.4237
9	Left middle frontal gyrus	0.4237
10	Left anterior cingulate and paracingulate gyri	0.4237
11	Left middle temporal gyrus	0.4237
12	Left inferior temporal gyrus	0.4237
13	Left temporal pole: middle temporal gyrus	0.3898
14	Right lenticular nucleus, putamen	0.3559
15	Right thalamus	0.3559

[a]The top 15 regions were selected just for illustration according to their *W*-score values. To be noted, more than 15 ROIs were used in our classification.

(AMYG), the bilateral middle temporal gyrus (MTG), the right inferior occipital gyrus (IOG), the left superior temporal gyrus of temporal pole (TPOsup), the bilateral middle temporal gyrus of temporal pole (TPOmid), the bilateral inferior temporal gyrus (ITG), the right putamen of lenticular nucleus (PUT), and the right thalamus (THA). In addition, for Δf, the selected regions also include the bilateral orbital part of superior frontal gyrus (ORBsup), the left middle frontal gyrus (MFG) and the left anterior cingulate and paracingulate gyri (ACG). For Δf+Hurst, the right paracentral lobule (PCL), the left superior temporal gyrus (STG), the right heschl gyrus (HES) and the right angular gyrus are also selected.

In addition, in Figure 5, the corresponding selected discriminative ROIs for both Δf and Δf+Hurst features were visualized against the cortical surface. It can be found that most of the selected discriminative ROIs for these two types of features are overlapped and show similar pattern in many regions.

DISCUSSION

In the present study, we investigated how to apply multifractal analysis on AD study with rs-fMRI data. To verify the multifractality in rs-fMRI time series, both BCMA and WLMA were used. BCMA is a classical multifractal tool which has been widely used, e.g., Perrier et al, Cuevas, and Wang et al (42–44), while WLMA is a recently proposed technique and is becoming popular in recent years (16,45,46). As shown in Figures 2b and 3, the existence of multifractal characteristics in cerebral ROIs had been validated by both methods. In Shimizu et al, Wink et al, and Ciuciu et al (12,15,16), multifractal properties were found in different brain regions of the healthy subjects. Our investigation is consistent with these previous studies and also extends to the AD subjects.

Based on MFS generated by BCMA, four canonical features, $\alpha(0)$, $\Delta\alpha$, Δf and P_c, were extracted. Compared with traditional features (i.e., Hurst exponent from monofractal analysis, ReHo, ALFF, and fALFF from linear indices, and wLCC from functional connectivity), the individual multifractal feature, Δf, showed the best classification performance to discriminate AD patients from healthy controls, with an accuracy of 69.49%, suggesting it possibly be a good marker to diagnose AD.

As described, Δf is a very important quantity, measuring the ratio between the regions with the most concentrated and the most rarified probabilities (32,33). In particular, the left skewed MFS with $\Delta f > 0$ shows there are more concentrated regions than rarified ones, whereas the right skewed MFS with $\Delta f < 0$ shows the contrary. In our study, on average, MFS on 69 ROIs for NC and 67 ROIs for AD had $\Delta f > 0$, suggesting that MFS was shaped as left skewness on over 74% ROIs, as illustrated in Figure 2a. It suggests that the signals are more statistically irregular and singular in these regions.

In addition, the classification performance can be substantially further improved when combining the multifractal features with other traditional features, especially for Δf+Hurst that achieves the classification accuracy up to 76.27% (see Tables 2 and 3). It is worth mentioning that although some multifractal features (e.g., $\alpha(0)$ and P_c) do not show strong discriminative power individually, they can still significantly improve the classification performance when combined with the monofractal, the linear or the network features (e.g. Hurst, ReHo, or wLCC). For example, although the accuracies of $\alpha(0)$ and ReHo as individual features are only around 55% in Table 2, the accuracy of $\alpha(0)$+ReHo, with appropriate combination weights obtained by MKL, can be boosted more than 15%, achieving 72% in Table 3. This may indicate that, there does exist complementary information between the multifractal features and the other ones, and the classification performance can benefit from such combinations.

As indicated in Yan et al (37), it might be less effective for ℓ_1-MKL when the combined kernels carry complementary but less overlapped information. This may explain the relatively inferior performance of ℓ_1-MKL to

Table 5
Top 15 ROIs Showing the Most Discriminative Power for Classification by Δf+Hurst Feature[a]

No.	Regions	*W*-score
1	Right temporal pole: middle temporal gyrus	0.6695
2	Right inferior temporal gyrus	0.6017
3	Left amygdale	0.5932
4	Right middle temporal gyrus	0.5763
5	Left inferior temporal gyrus	0.5593
6	Left temporal pole: superior temporal gyrus	0.5169
7	Left temporal pole: middle temporal gyrus	0.5169
8	Right lenticular nucleus, putamen	0.5085
9	Right thalamus	0.5085
10	Right inferior occipital gyrus	0.4068
11	Right paracentral lobule	0.3898
12	Left middle temporal gyrus	0.3814
13	Left superior temporal gyrus	0.3729
14	Right angular gyrus	0.3220
15	Right heschl gyrus	0.3220

[a]The top 15 regions were selected just for illustration according to their *W*-score values. To be noted, more than 15 ROIs were used in our classification.

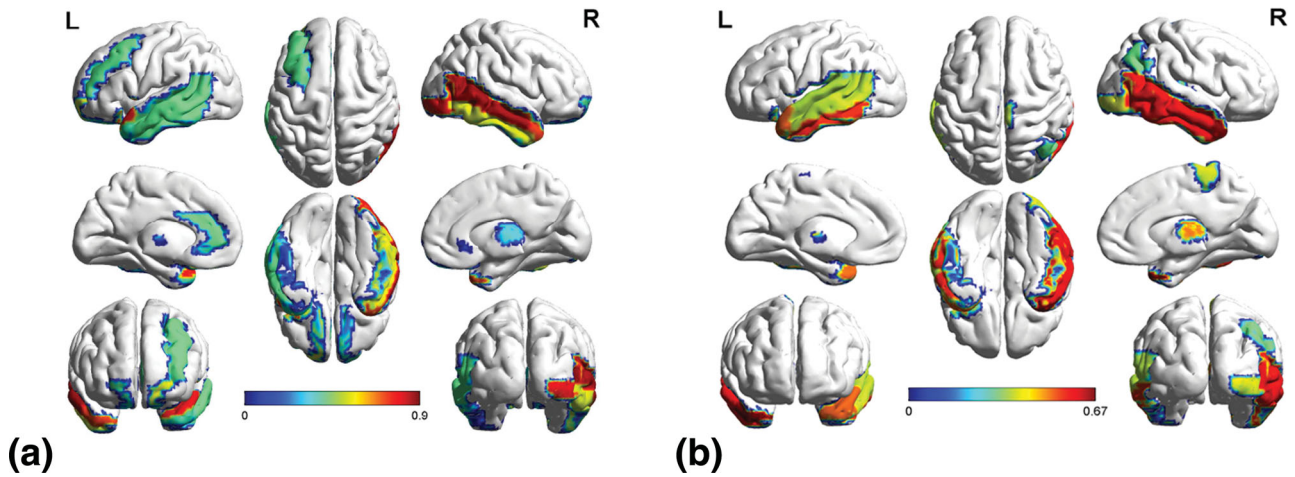

FIG. 5. The top 15 ROIs with the most discrimination power projected onto the cortical surface (**a**) for Δf; (**b**) for Δf+Hurst.

other nonsparse MKL formulations, observed in our experiments. Moreover, most of the best classification performances on combined features were obtained by ℓ_2-MKL and ℓ_3-MKL, indicating the necessity of considering nonsparse ℓ_p-MKL in such kinds of study rather than merely focusing on sparse ℓ_1-MKL only.

Because it is not straightforward to find the appropriate kernel for classification, many researchers turned to using multiple kernel types instead of a single one and tried to find the optimal combination of them (34). The used kernels could correspond to different similarity measures or different feature sources. In our experiment, five different kernels and four different combination configurations were explored. In Table 3, most of the best classification results are obtained by using GRBF+Poly, suggesting the robustness of this kernel combination for discriminating AD from NC.

Our investigation identified ROIs that are discriminative between AD and NC groups. These ROIs are from both brain hemispheres and mainly cover part of the limbic lobe, most of the temporal lobe, part of the frontal lobe and part of the parietal lobe. They are consistent with previous studies that used conventional univariate statistical analysis for AD detection. For example, as reported in Schafe et al (47), the AMYG is part of the limbic system that AD mainly affects. Statistical analysis in Poulin et al (48) showed that the magnitude of AMYG atrophy is comparable to that of the hippocampus in the earliest clinical stages of AD, and is related to global illness severity. In Binnewijzend et al (49), the increased eigenvector centrality (EC) in the ACG was found in AD patients by using rs-fMRI data, which is associated with cognitive performance and AD pathology. Scheff et al (50) found that the ITG plays an important role in verbal fluency, a cognitive function affected early in the onset of AD. More recently, the study in Sturm et al (51) reported that higher emotional contagion in AD is associated with smaller volume in the right ITG, MTG, STG, the right TPO, anterior hippocampus, parahippocampal gyrus, and left MTG. Generally, these previous studies support that our identified ROIs are closely related to AD and reasonably discriminative for AD diagnosis.

Additionally, the integration of multiple modalities of data, such as MRI, positron emission tomography, and diffusion tensor imaging etc., has been recently studied for AD classification. However, multiple complementary features can also be extracted from a single modality to improve the classification performance, as demonstrated by our work. For example, the features from multifractal analysis and those from connectivity analysis, can be both extracted from rs-fMRI and integrated to improve the disease classification accuracy, even without additional information from other modalities. Compared with structural data, functional data has its own advantages especially for the conditions that lack brain structural abnormalities (52). Therefore, it is of great benefit to sufficiently exploit the potential of fMRI data from multiple perspectives. That is one of the purposes of exploring different features on fMRI data in this study.

The current study is limited by the following factors. First, the time point used for multifractal analysis in the current study is relatively short, although this is a typical configuration in the widely used ADNI dataset. Further investigations on longer rs-fMRI data will be our future work. Meanwhile, a new wavelet-based method, the maximal overlap discrete wavelet transform (MODWT) (53) is also worthy of exploration. MODWT removes the restriction that the series length has to be the power of 2, and is insensitive to the beginning of the time series, which thus has advantages over WLMA. We will integrate MODWT into our multifractal analysis framework and validate its performance in future. Second, our current study is limited by the small number of AD subjects, which may affect its generalization. Therefore, a validation of our method on larger AD datasets should be further conducted. Third, an appropriate brain parcellation is critical to properly capture functional regions in the brain. Therefore, our work may benefit from a brain atlas obtained directly from functional images rather than the AAL atlas rooted in anatomical images. Finally, the integration of imaging modalities other than rs-fMRI may further improve the classification performance and will be explored in the future.

CONCLUSIONS

In this article, we systematically investigated the discriminative power of multifractal features on rs-fMRI data with regard to AD, and compared them with the monofractal, linear and network-based features. The multifractal feature, Δf, outperforms other features when used individually. Furthermore, we showed that the classification accuracy can be dramatically improved when combining these multifractal features with other features by the MKL technique. Our work demonstrated the potential usefulness of multifractal analysis for AD research, especially when combining with the traditional rs-fMRI features. It contributes to distinguishing AD from NC subjects.

ACKNOWLEDGMENTS

We thank the support from the State Scholarship Fund of China Scholarship Council (CSC), the Vice Chancellor Research Grant in University of Wollongong, and the project funded by the Priority Academic Program Development of Jiangsu Higher Education Institutions (PAPD). All authors report no potential conflict of interest.

REFERENCES

1. Salloway S, Correia S. Alzheimer disease: time to improve its diagnosis and treatment. Clev Clin J Med 2009;76:49–58.
2. Biswal B, Zerrin Yetkin F, Haughton VM, Hyde JS. Functional connectivity in the motor cortex of resting human brain using echo-planar MRI. Magn Reson Med 1995;34:537–541.
3. Fox MD, Raichle ME. Spontaneous fluctuations in brain activity observed with functional magnetic resonance imaging. Nat Rev Neurosci 2007;8:700–711.
4. Chen G, Ward BD, Xie C, Li W, Wu Z, Jones JL, Franczak M, Antuono P, Li S. Classification of Alzheimer disease, mild cognitive impairment, and normal cognitive status with large-scale network analysis based on resting-state functional MR imaging. Radiology 2011;259:213.
5. Greicius MD, Srivastava G, Reiss AL, Menon V. Default-mode network activity distinguishes Alzheimer's disease from healthy aging: evidence from functional MRI. Proc Natl Acad Sci U S A 2004;101:4637–4642.
6. He Y, Wang L, Zang Y, Tian L, Zhang X, Li K, Jiang T. Regional coherence changes in the early stages of Alzheimer's disease: a combined structural and resting-state functional MRI study. Neuroimage 2007;35:488–500.
7. Li S, Li Z, Wu G, Zhang M, Franczak M, Antuono PG. Alzheimer disease: evaluation of a functional MR imaging index as a marker. Radiology 2002;225:253–259.
8. Han Y, Wang J, Zhao Z, Min B, Lu J, Li K, He Y, Jia J. Frequency-dependent changes in the amplitude of low-frequency fluctuations in amnestic mild cognitive impairment: a resting-state fMRI study. Neuroimage 2011;55:287–295.
9. Wang K, Liang M, Wang L, Tian L, Zhang X, Li K, Jiang T. Altered functional connectivity in early Alzheimer's disease: a resting-state fMRI study. Hum Brain Mapp 2007;28:967–978.
10. Maxim VC, CSendur L, Fadili J, Suckling J, Gould R, Howard R, Bullmore E. Fractional Gaussian noise, functional MRI and Alzheimer's disease. Neuroimage 2005;25:141–158.
11. Zarahn E, Aguirre GK, D'Esposito M. Empirical analyses of BOLD fMRI statistics. Neuroimage 1997;5:179–197.
12. Shimizu Y, Barth M, Windischberger C, Moser E, Thurner S. Wavelet-based multifractal analysis of fMRI time series. Neuroimage 2004;22:1195–1202.
13. Suckling J, Wink AM, Bernard FA, Barnes A, Bullmore E. Endogenous multifractal brain dynamics are modulated by age, cholinergic blockade and cognitive performance. J Neurosci Methods 2008;174:292–300.
14. Achard S, Bassett DS, Meyer-Lindenberg A, Bullmore E. Fractal connectivity of long-memory networks. Phys Rev E Stat Nonlin soft Matter Phys 2008;77:036104.
15. Wink A, Bullmore E, Barnes A, Bernard F, Suckling J. Monofractal and multifractal dynamics of low frequency endogenous brain oscillations in functional MRI. Hum Brain Mapp 2008;29:791–801.
16. Ciuciu P, Varoquaux G, Abry P, Sadaghiani S, Kleinschmidt A. scale-free and multifractal time dynamics of fMRI signals during rest and task. Front Physiol 2012;3:186.
17. Lopes R, Betrouni N. Fractal and multifractal analysis: a review. Med Image Anal 2009;13:634–649.
18. Goldberger AL, Rigney DR, West BJ. Chaos and fractals in human physiology. Sci Am 1990;262:42–49.
19. Haller S, Lovblad KO, Giannakopoulos P. Principles of classification analyses in mild cognitive impairment (MCI) and Alzheimer disease. J Alzheimers Dis 2011;26:389–394.
20. LaConte SM, Peltier SJ, Hu XP. Real-time fMRI using brain-state classification. Hum Brain Mapp 2007;28:1033–1044.
21. Wang K, Jiang T, Liang M, Wang L, Tian L, Zhang X, Li K, Liu Z. Discriminative analysis of early Alzheimer's disease based on two intrinsically anti-correlated networks with resting-state fMRI. Med Image Comput Assist Interv 2006;9(Pt 2):340–347.
22. Tripoliti EE, Fotiadis DI, Argyropoulou M. A supervised method to assist the diagnosis and monitor progression of Alzheimer's disease using data from an fMRI experiment. Artif Intell Med 2011;53:35–45.
23. Dai Z, Yan C, Wang Z, Wang J, Xia M, Li K, He Y. Discriminative analysis of early Alzheimer's disease using multi-modal imaging and multi-level characterization with multi-classifier (M3). Neuroimage 2012;59:2187–2195.
24. Hinrichs C, Singh V, Xu G, Johnson S. MKL for robust multi-modality AD classification. Med Image Comput Assist Interv 2009;12(Pt 2):786–794.
25. Chao-Gan Y, Yu-Feng Z. DPARSF: a MATLAB toolbox for "pipeline" data analysis of resting-state fMRI. Front Syst Neurosci 2010;4:13.
26. Friston KJ, Holmes AP, Worsley KJ, Poline J, Frith CD, Frackowiak RS. Statistical parametric maps in functional imaging: a general linear approach. Hum Brain Mapp 1994;2:189–210.
27. Tzourio-Mazoyer N, Landeau B, Papathanassiou D, Crivello F, Etard O, Delcroix N, Mazoyer B, Joliot M. Automated anatomical labeling of activations in SPM using a macroscopic anatomical parcellation of the MNI MRI single-subject brain. Neuroimage 2002;15:273–289.
28. Wendt H, Abry P, Jaffard S. Bootstrap for empirical multifractal analysis. IEEE Signal Process Mag 2007;24:38–48.
29. Muzy JC, Bacry E, Arneodo A. Multifractal formalism for fractal signals: the structure-function approach versus the wavelet-transform modulus-maxima method. Phys Rev E 1993;47:875.
30. Jaffard S. Wavelet techniques in multifractal analysis. In: Lapidus ML, VanFrankenhuijsen M, editors. Proceedings of Symposia in Pure Mathematics. Providence: American Mathematical Society (Volume 72); 2004. p 91–151.
31. Lashermes B, Jaffard S, Abry P. Wavelet leader based multifractal analysis. In: Acoustics, speech, and signal processing, 2005. Proceedings. (ICASSP '05). IEEE International Conference on Acoustics, Speech, and Signal Processing (Volume 4); 2005. p 161–164.
32. Chhabra A, Jensen RV. Direct determination of the f (α) singularity spectrum. Phys Rev Lett 1989;62:1327–1330.
33. Halsey TC, Jensen MH, Kadanoff LP, Procaccia I, Shraiman BI. Fractal measures and their singularities: the characterization of strange sets. Phys Rev A 1986;33:1141.
34. Fayao L, Luping Z, Chunhua S, Jianping Y. Multiple kernel learning in the primal for multimodal Alzheimer's disease classification. IEEE J Biomed Health Inform 2014;18:984–990.
35. Hinrichs C, Singh V, Xu G, Johnson SC. Predictive markers for AD in a multi-modality framework: an analysis of MCI progression in the ADNI population. Neuroimage 2011;55:574–589.
36. Rakotomamonjy A, Bach FR, Canu S, Grandvalet Y. SimpleMKL. J Mach Learn Res 2008;9:2491–2521.
37. Yan F, Mikolajczyk K, Kittler J, Tahir M. A comparison of L1 norm and L2 norm multiple kernel SVMs in image and video classification. Content-based multimedia indexing, 2009. CBMI '09. Seventh International Workshop on. Chania; 2009. p 7–12.
38. Kloft M, Brefeld U, Sonnenburg S, Zien A. Lp-norm multiple kernel learning. J Mach Learn Res 2011;12:953–997.

39. Kloft M, Brefeld U, Laskov P, Sonnenburg S. Non-sparse multiple kernel learning. In: NIPS Workshop on Kernel Learning: automatic selection of optimal kernels. Whistler, Canada; 2008.
40. Lahmiri S, Boukadoum M. Automatic detection of Alzheimer disease in brain magnetic resonance images using fractal features. In 6th International IEEE/EMBS Conference on Neural Engineering (NER). San Diego, CA; 2013. p 1505–1508.
41. Wee CY, Yap PT, Zhang D, Wang L, Shen D. Constrained sparse functional connectivity networks for MCI classification. Med Image Comput Assist Interv 2012;15(Pt 2):212–219.
42. Perrier E, Tarquis AM, Dathe A. A program for fractal and multifractal analysis of two-dimensional binary images: computer algorithms versus mathematical theory. Geoderma 2006;134:284–294.
43. Cuevas E. f (α) multifractal spectrum at strong and weak disorder. Phys Rev B 2003;68:24206.
44. Wang J, Ning X, Ma Q, Bian C, Xu Y, Chen Y. Multiscale multifractality analysis of a 12-lead electrocardiogram. Phys Rev E 2005;71: 62902.
45. Van de Ville D, Britz J, Michel CM. EEG microstate sequences in healthy humans at rest reveal scale-free dynamics. Proc Natl Acad Sci U S A 2010;107:18179–18184.
46. Ciuciu P, Abry P, Rabrait C, Wendt H. Log wavelet leaders cumulant based multifractal analysis of EVI fMRI time series: evidence of scaling in ongoing and evoked brain activity. IEEE J Sel Top Signal Process 2008;2:929–943.
47. Schafe GE, Doyère V, LeDoux JE. Tracking the fear engram: the lateral amygdala is an essential locus of fear memory storage. J Neurosci 2005;25:10010–10014.
48. Poulin SP, Dautoff R, Morris JC, Barrett LF, Dickerson BC. Amygdala atrophy is prominent in early Alzheimer's disease and relates to symptom severity. Psychiatry Res 2011;194:7–13.
49. Binnewijzend MA, Adriaanse SM, Flier WM, Teunissen CE, Munck JC, Stam CJ, Scheltens P, Berckel BN, Barkhof F, Wink AM. Brain network alterations in Alzheimer's disease measured by Eigenvector centrality in fMRI are related to cognition and CSF biomarkers. Hum Brain Mapp 2014;35:2383–2393.
50. Scheff SW, Price DA, Schmitt FA, Scheff MA, Mufson EJ. Synaptic loss in the inferior temporal gyrus in mild cognitive impairment and Alzheimer's disease. J Alzheimers Dis 2011;24:547–557.
51. Sturm VE, Yokoyama JS, Seeley WW, Kramer JH, Miller BL, Rankin KP. Heightened emotional contagion in mild cognitive impairment and Alzheimer's disease is associated with temporal lobe degeneration. Proc Natl Acad Sci U S A 2013;110:9944–9949.
52. Dosenbach NU, Nardos B, Cohen AL, et al. Prediction of individual brain maturity using fMRI. Science 2010;329:1358–1361.
53. Percival DB, Guttorp P. Long-memory processes, the Allan variance and wavelets. In: Foufoula-Georgiou E, Kumar P, editors. Wavelets in geophysics. San Diego: Academic Press; 1994. p 325–344.

SUPPORTING INFORMATION

Additional Supporting Information may be found in the online version of this article.

Figure S1. Illustration diagram of discriminative feature selection and the leave-one-out (LOO) classification scheme. The pink arrows in the LOO box indicate the process of identifying the discriminative ROI (see the Discriminative Feature Selection section), and the black arrows in the LOO box indicate the process of classification. The mark sROI in the LOO box denotes as "selected ROI", while ACC, SEN, and SPE denote as accuracy, sensitivity, and specificity, respectively.

Figure S2. Illustration of the performance of WLMA and BCMA with respect to the length of binomial multiplicative simulation data for multifractal characteristics verification. **a**: Boxplots of c_2 values for WLMA with the resample number of 49. The horizontal axis corresponds to the series length ranging from 2^6 to 2^{15}, while the vertical axis corresponds to the estimate of c_2 value. The solid dots represent the outliers observed for two lengths. The dash-dot line at $c_2 = 0$ is plotted as a reference. Including $c_2 = 0$ suggests denying the multifractal characteristics. **b**: Slopes of three lines with $q = 1, 2, 3$ for BCMA. The horizontal axis corresponds to the series length, while the vertical axis corresponds to the slope values. The presence of three different slope values demonstrates the existence of multifractal characteristics.